Check for updates

Damage evolution of the coating/substrate system TiN/X2CrNi18-9 under high indentation loads: experimental and numerical study

Amir Bahri[iD] · **Manel Ellouz** · **Michaela Klöcker** ·
Khaled Elleuch · **Thomas Kordisch**

Abstract Hard coatings, in particular TiN, are widely used as coatings for cutting tools and in the agri-food industry. In the literature, however, few characterizations of hard coatings can be found which define the minimum applied load when the coating starts to fail. In the present study TiN coating was deposited on stainless steel X2CrNi18-9. Vickers and Brinell indentation tests with a wide load range were performed. The main results revealed that the increase of the applied load in Vickers and Brinell indentation influenced the coating and coating/substrate damage evolution. SEM investigation of the Vickers indentation area shows five modes of damage: inclined cracks, radial cracks, lateral cracks, edge cracks, and shear steps. Each damage mode occurs at a specific load range. Parallel cracks already appeared at the edges of the indents at the lowest load of 2 N. For Brinell indentation, cracks start in the coating only at loads higher than F = 307 N. The SEM examinations present damage modes such as circumferential cracks in the border and additional circular cracks in the center of the indent, creating a crack network. Numerical simulations of Brinell indentation were carried out in order to determine the stress distribution in the indent. The comparison of the numerical simulation results with the experimental findings revealed that the coating started to fail at a stress range above 5735 MPa which corresponds to a normal load range of higher than 307 N in Brinell indentation tests. At a load of 613 N cracks were observed.

A. Bahri (✉) · M. Ellouz · M. Klöcker · T. Kordisch
Laboratory for Materials Testing, Bielefeld Institute
for Applied Materials Research (BIfAM), University
of Applied Sciences Bielefeld, Interaction 1,
33619 Bielefeld, Germany
e-mail: amir.bahri@fh-bielefeld.de

M. Ellouz
e-mail: manel.ellouz@fh-bilelfeld.de

M. Klöcker
e-mail: michaela.kloecker@fh-bielefeld.de

T. Kordisch
e-mail: thomas.kordisch@fh-bielefeld.de

K. Elleuch
Laboratory of Materials Engineering and Environment
(LGME), National Engineering School of Sfax, University
of Sfax, B.P.W.1173, 3038 Sfax, Tunisia
e-mail: khaled.elleuch@enis.tn

1 Introduction

Hard PVD coatings, in particular TiN, show good tribological properties and are therefore increasingly used in different mechanical areas (Jianxin et al. 2012; Bahri et al. 2015, 2018; Bahri et al. 2016a, b), especially for cutting tools (Bobzin 2017; Vereschaka et al. 2017; Arulkirubakaran et al. 2017) and for applications in the agro-alimentary industry (Bahri

🖄 Springer

et al. 2015; Bahri et al. 2016a, b). Nevertheless, the selection of such coatings for specific applications depends on many factors, i.e., the interface quality of the bonding between the coating and the substrate, the surface morphology of the coating and the expected lifetime under service loading conditions. Mechanical properties, such as Young's modulus and hardness, in combination with loading conditions influence the damage behaviors of hard coatings (Bahri et al. 2015; Arulkirubakaran et al. 2017; Bell et al. 1998). The damage behavior of the TiN coating is still presented as a challenge for determining the critical load at which the coating starts to fail and the type of damage mode occurring throughout the coating. Several experimental and numerical researches were conducted to analyse fracture throughout metallic materials (Kim et al. 2004; Martinez et al. 2015; Ducobu et al. 2017; Zhang et al. 2019, 2021; Singh et al. 2011; Ren et al 2019, 2020). Kim et al. reported in their research about cracks propagation in graded materials that the crack simulation was performed in mixed mode loadings conditions. The cracks propagation and the deformation were conducted under a purely elastic behavior (Kim et al. 2004). Furthermore, Martinez et al. focused their attention to study the numerical simulation limits to reproduce the real damage throughout materials (Martinez et al. 2015). Extended finite elements method (XFEM) was adopted during study. They mentioned that prediction of crack propagation path by finite element codes is possible only using local crack propagation criteria.

Indentation testing presents an important method for characterizing a material's mechanical properties because of the simplicity of preparing samples and conducting tests (Bahri et al. 2019; Baoxing et al. 2010). The indentation test is based on the penetration of an indenter into the target materials, which provides a load–penetration curve. Several researchers have used indentation tests to determine the hardness, Young's modulus, and damage modes of several coatings (Bahri et al. 2018, 2019). Other authors concentrated their efforts on correlating the load–penetration curve obtained by indentation to the material's elastic–plastic behavior, which is represented by a classic uniaxial stress−strain curve (Baoxing et al. 2010). Some researchers focused on determining the mechanical properties and the damage behaviors (Kot et al. 2013; Vadiraj et al. 2006; Yongqiang et al. 2017). Kot et al. (Kot et al. 2013)

focused on determining the stress−strain curve of a TiN coating by using a combined numerical and experimental indentation methodology in which the critical stress for fracture and the damage evolution of the coating-substrate systems were determined. According to the literature (Bhowmick et al. 2003), under Vickers and Brinell indentation tests, the damage modes occurring throughout the coating are inclined cracks, lateral cracks, and shear steps (see Fig. 1). Some authors (Vadiraj et al. 2006; Yongqiang et al. 2017; Bhowmick et al. 2003) used nanoindentation, in particular, to characterize hard coatings. Moreover, the researchers did not consider the material's response under high loads. According to the literature review, the use of Brinell and Vickers indentation techniques (Koike et al. 2012; Perzynski et al. 2013; Cao et al. 2007) is an adequate method for analyzing and characterizing substrate materials and hard coatings. Nevertheless, few researchers investigated how the damage modes of the coating are influenced by the mechanical properties of the coating and substrate (Pantel et al. 2012; Tasdemirci et al. 2015; Bahri et al. 2016a, b) and by the geometry of the indenter.

Several researchers attributed PVD coatings, such as TiN, to purely elastic behavior (Kot et al. 2013; Bhowmick et al. 2003; Faisal et al. 2017; Lee et al. 1998) and others to elastic–plastic behavior (Kopernik et al. 2011; Dejun et al. 2015). Furthermore, to the author's knowledge, several researches (Bhowmick et al. 2003; Faisal et al. 2017) analyzed the damage taken place throughout the TiN coating,
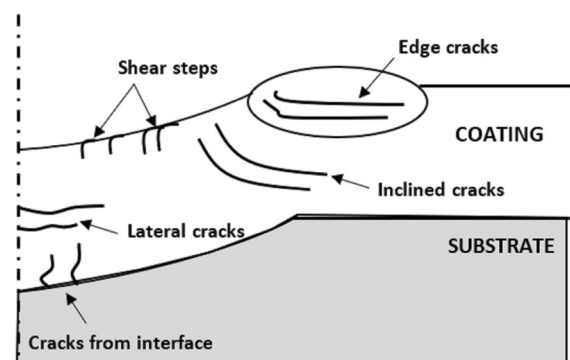

Fig. 1 Schematic illustrations of the damage modes throughout the coating under the indentation test (Bhowmick et al. 2003)

however, the relation between the damage and the mechanical properties is still unclear.

In this study, a TiN coating is deposited on stainless steel X2CrNi18-9 using the cathodic arc physical vapor deposition (CAPVD) technique. Vickers and Brinell indentation tests are conducted to determine the effects of the tests and the applied loads on the damage modes throughout the coating. In this study, the main purpose is to determine the damage modes of the coating while considering additionally the influence of the substrate material. Therefore, high loads, occurring in industrial applications, are applied within both indentation methods, knowing that high loads are not appropriate to investigate the pure coating because of the high indentation depths. Furthermore, a numerical study is conducted to determine the stress distribution within the coating/substrate system caused by the Brinell indentation. Based on this numerical study, the observed damage modes and especially the start of the first crack are correlated with the calculated stress distribution to prove the experimental findings. The main advantage of the numerical simulation in our study is the possibility of evaluating the stress distribution under loading and after the unloading phase. The stress range of the first crack initiation is determined by correlating the residual stress distribution throughout the coating after unloading with the SEM images of the indents. Assuming that the cracks initiate and grow throughout the coating under the loading phase, the results of the stress distribution under the loading phase are provided. Innovation of the paper is to put a head about the geometric effect (Vickers and Brinell configuration) on the damage mode of the coating. And the second issue is that the damage type (circumferential crack, radial crack, network crack, etc.) could change for the same material depending on the loading value.

2 Materials and methods

2.1 Experimental procedure

TiN coating was deposited on the stainless steel X2CrNi18-9 using CAPVD. The substrate with dimensions of $30 \times 30 \times 2.8$ mm^3 was cleaned and polished before being introduced into the vacuum chamber. During the CAPVD process, a water-cooled metallic titanium cathode was used. The coating was deposited with continuous current (DC-150 V) under an average temperature of 640 °C. More details about the procedure could be found in previous studies (Bahri et al. 2015, 2018; Bahri et al. 2016a, b). Notably, to obtain good adhesion of the coating, a pure Ti layer was deposited first. The Ti layer was deposited between the coating and the substrate. Using the Calotest technique, the TiN coating thickness was measured, resulting in an average value of 4.17 μm (Bahri et al. 2015; Bahri et al. 2016a, b).

A tensile test was conducted on the substrate material using an Instron 8802 universal machine. In Fig. 2, the stress−strain curve of the substrate material X2CrNi18-9 is given to be later introduced in the numerical analysis. The substrate X2CrNi18-9 was characterized by a Young's modulus of 188 GPa, and reached a tensile strength of 737 MPa.

The Brinell indentation test was performed using the Zwick ZHU 2.5 device with a 2.5 mm carbide ball, as presented in previous studies (Bahri et al. 2018, 2019). The Vickers test was carried out with a pyramidal diamond indenter. Figure 3 illustrates a schematic configuration of the conducted indentation tests. Wide ranges of normal loads between 10 and 613 N were applied for the Brinell indentation test and between 2 and 200 N for the Vickers indentation test. Indentations were carried out with a velocity V = 1 mm/min. For good reproductivity of the results, all tests were performed at least three times.

SEM images were taken using SEM ZEISS 1450 VPSE to determine the coating morphology and the damage modes.

2.2 Finite element modeling of the Brinell indentation test

The numerical model representing the Brinell test was built based on a previous study using ABAQUS (Bahri et al. 2019). The indentation test setup was reproduced by a 4×3 mm^2 axisymmetric model of stainless steel X2CrNi18-9 coated by TiN. The model design, mesh, and boundary conditions are shown in Fig. 4. The stainless steel X2CrNi18-9 was constrained at the bottom surface. X2CrNi18-9 adopted an elastic–plastic behavior in the simulation, obtained by the experimental stress−strain curve in Fig. 2. A tie relationship was used in the interface of the coating/substrate. During the simulation, a standard static

Fig. 2 Stress–strain curve of the stainless steel X2CrNi18-9
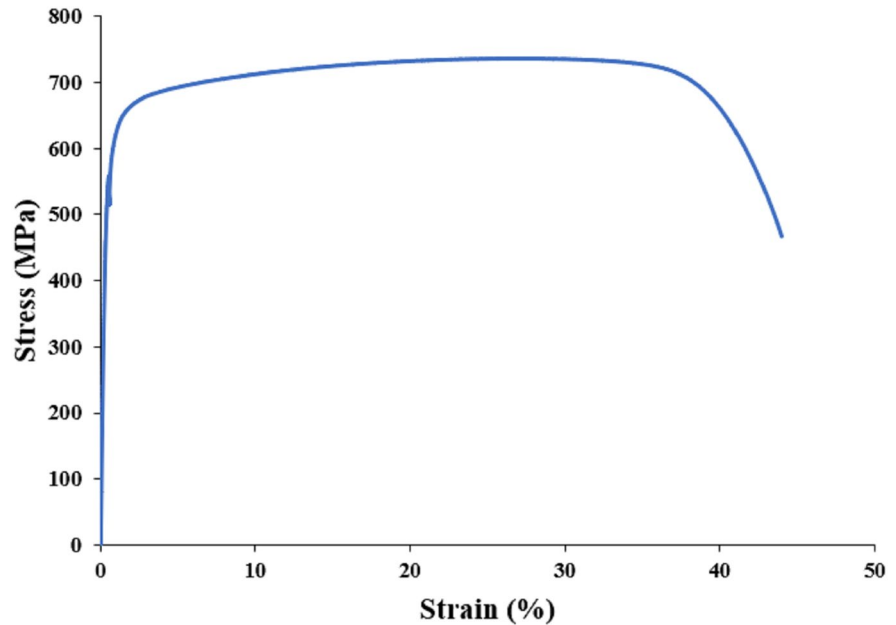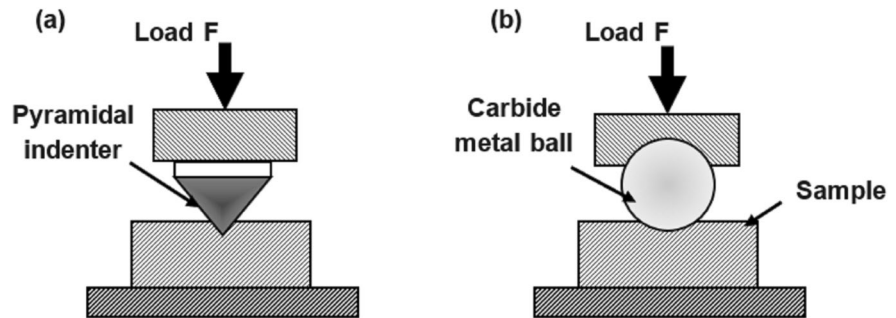

Fig. 3 Schematic configuration of the indentation test: **a** Vickers and **b** Brinell (Bahri et al. 2018)

calculation mode was considered. The axis-symmetric model was considered to reduce calculation time. The total numbers of elements and nodes were 3336 and 3640, respectively. A 4-node bilinear axisymmetric quadrilateral element with reduced integration, that was optimized by an hourglass control (CAX4R), was used. The TiN coating was considered as a purely elastic material with a Young's modulus of E = 297 GPa and a Poisson's coefficient of $\nu = 0.3$; these parameters were determined by microindentation measurements performed by the company Anton-Paar using a STEP500-NHT[3]-MCT[3] nano/microindenter. The TiN coating was modeled with a thickness e = 4.17 μm. Note that the Ti layer was not considered in this simulation since it was only a few nanometers thick and its role was to create adhesion between the TiN coating and the stainless steel substrate.

Additionally, note that a mesh refinement was used in the contact zone and throughout the thickness of the TiN coating for the accuracy of the results. The Brinell indenter was modeled as an analytical rigid body. The contact properties between the indenter and the TiN coating were considered frictionless. In the first step, the simulation was conducted with respect to the Hertz conditions to validate the numerical model. It is worth clarifying that a maximum penetration of 4.7×10^{-2} μm was applied, presenting a depth 100 times lower than the thickness of the TiN coating. The analytical contact pressure profile was calculated and compared with the numerical profile to validate the numerical model. The contact pressure profile was calculated using Eq. (1) (Johnson 1987), where r is the distance from the center of the indent, $p_0 = \frac{2aE^*}{\pi R}$ is the maximum contact pressure, a is the

Fig. 4 Numerical model: **a** model design and **b** mesh refinement and boundary conditions
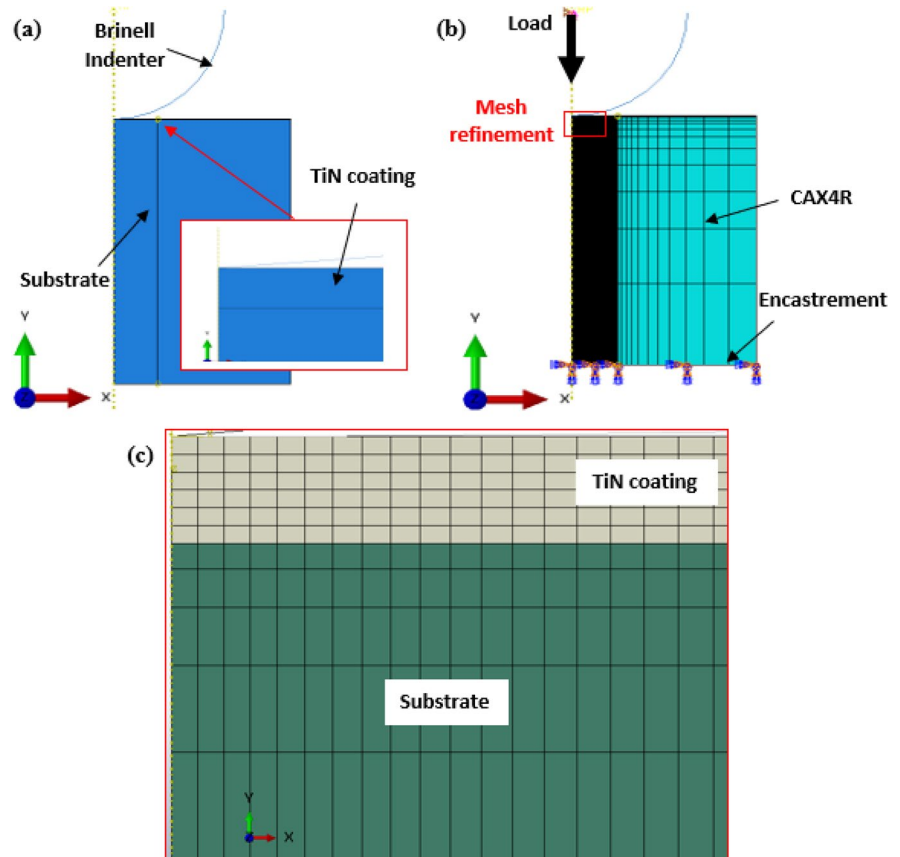
contact radius, E^* is the reduced Young's modulus and R is the indenter radius.

$$p(r) = p_0 \sqrt{1 - \left(\frac{r}{a}\right)^2} \qquad (1)$$

In a second step, numerical investigations were conducted with the purpose of understanding the stress distribution throughout the TiN/X2CrNi18-9 system, especially under high normal loads showing an influence of the substrate on the stress distribution in the coating.

3 Results and discussion

3.1 Experimental analysis

3.1.1 TiN coating morphology, structure, and mechanical properties

Figure 5 illustrates the typical morphology of the TiN coating surface as relatively smooth and uniform. On the top surface, numerous distinct white droplets were detected, as seen in Fig. 5a, which is a typical defect of the cathodic arc physical vapor deposition technique. The droplets were formed due to the evaporation of metal macroparticles, which could not adequately react with nitrogen during coating deposition (Liu et al. 2012). The cross-sectional view (Fig. 5b) showed a uniform coating and good adhesion between the coating and the substrate. Further characterizations by XRD (X-ray diffraction) revealed, as shown in Fig. 6, a preferred orientation of (111); this orientation resulted in the

Fig. 5 Coating morphology
and structure: **a** top coating
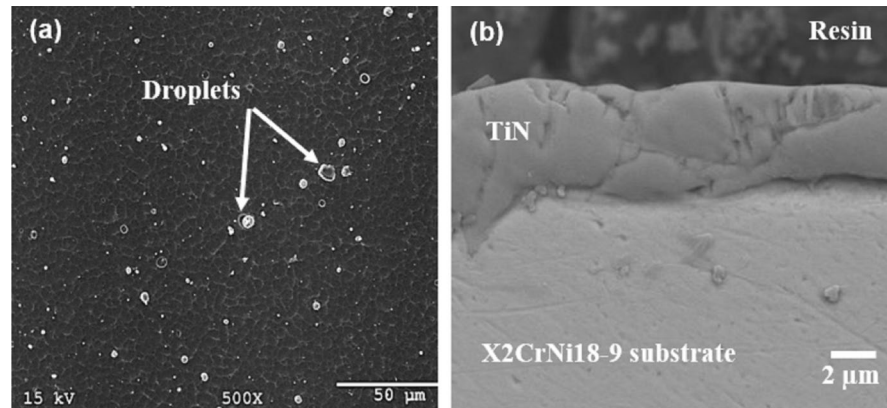surface (Bahri et al. 2015)
and **b** cross-section

Fig. 6 XRD θ–2θ measurements of the TiN coating
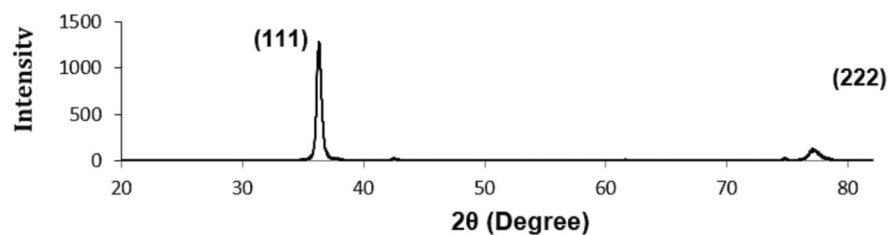(Bahri et al. 2015)

Table 1 Mechanical properties of TiN based on Vickers
microindentation tests using a load of 500 mN, realized by
Anton Paar Germany

Young's modulus (GPa)	Hardness (GPa)
297 ± 17	35

highest mechanical properties, mixed with fewer
(222) orientations, as reported in a previous study
(Bahri et al. 2015). Before conducting a wide range
of Brinell indentation tests on the TiN/X2CrNi18-9
system, the mechanical properties of the TiN coating were determined through a microindentation
test to be used in the finite element study. The main
results are presented in Table 1. It is important to
note that based on previous studies (Harris et al.
2004; Bahri et al. 2015; Bahri et al. 2016a, b), the
droplets present pure titanium which were not perfectly adhered to the coating during deposition.
Harris et al. proved in their study that the presence
of the droplets can affect the mechanical properties
of the coatings and the tribological performance.
The coating adopted in the current study exhibits
a very low percentage of droplets which appear at
the top surface (Bahri et al. 2015). Consequently,

the droplets may not have any influence on the compression modes during indentation.

3.1.2 TiN coating under Vickers indentation test

Figure 7 illustrates the load–unload curves of Vickers indentation starting from F = 2 N until F = 200 N.
The superposition of the load–unload curves showed
a very good fitting of the loading component. The
minimum applied load of F = 2 N led to an average
maximum indenter penetration of 5.7 μm, and the
maximum applied load of F = 200 N to 67 μm. The
lowest load of F = 2 N led to a penetration higher than
the coating thickness; thus, the substrate material
significantly influenced the Vickers penetration tests
at all applied loads. By analyzing the load curves at
F = 2 N, F = 3 N and F = 5 N (Fig. 7b), a slight change
in the slope evolution could be seen (marked by the
red arrows), which presented the so-called pop-ins
phenomenon; this phenomenon could be related to
the propagation of cracks throughout the TiN coating
(Peng et al. 2019). The pop-ins phenomenon occurred
due to the presence of an area with high tensile stress
concentrations, which could be the origin of the crack
initiation or delamination of the substrate/coating system (Wo et al. 2010; Weppelmann et al. 1994; Rabe
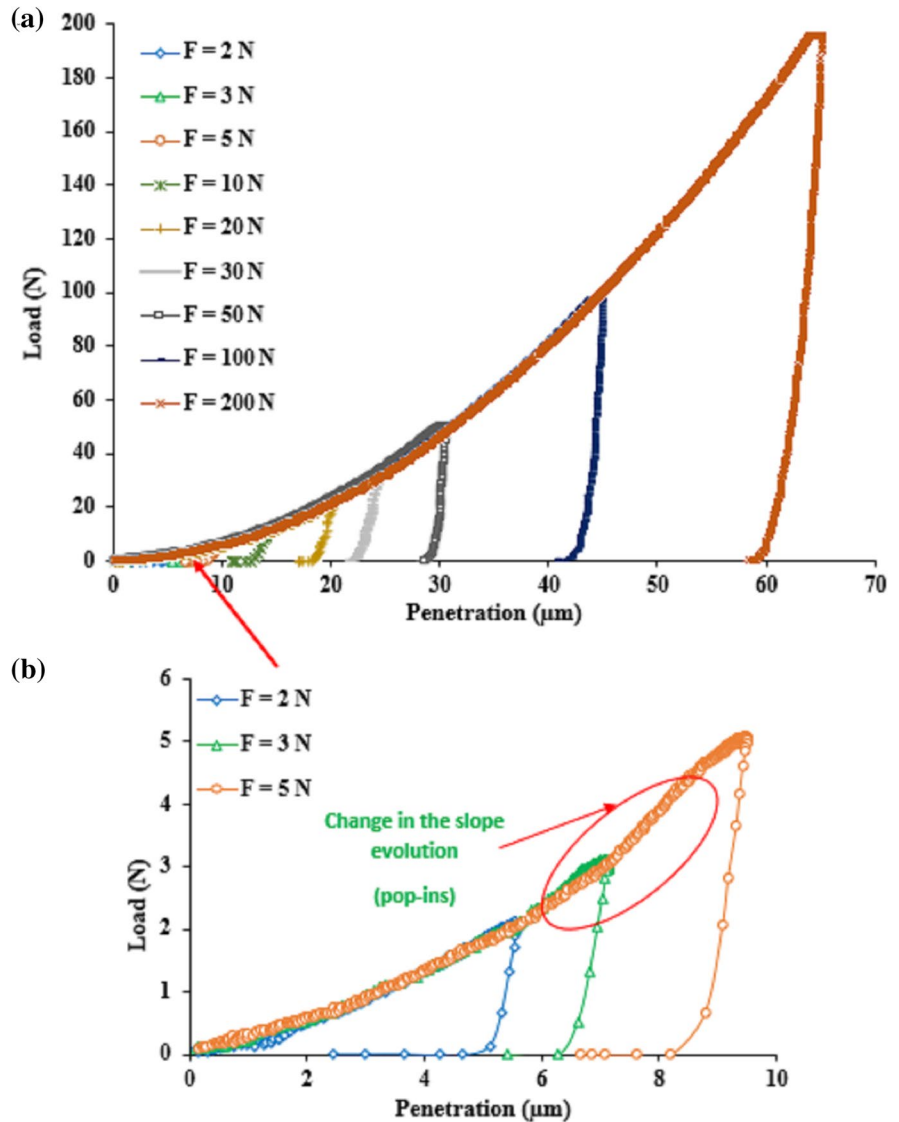
et al. 2004). In this case, the pop-in phenomenon was observed only at the load curve, resulting in a small change in the slope. According to the coating structure, the observed small pop-ins could be explained by crack initiation or the effect of other minor damages throughout the coating, as mentioned in previous studies (Weppelmann et al. 1994; Richter 2003). The effects of substrate plastic deformation on the measured values were more pronounced for higher loads, which affected the shape of the unloading curve.

Vickers indents were analyzed by SEM, and the results are shown in Fig. 8; these indentation results were the most important, and they will be discussed in the following paragraph. The diagonal (di) and the final penetration depths (hf) for the TiN coating reached 35 μm and 4.6 μm, respectively, at the minimum applied load F=2 N. Both (di) and (hf) increased with increasing normal load to reach 425 μm and 60 μm, respectively, at F=200 N. Note that the damage of the TiN coating (thickness of 4.17 μm) already occurred at the lowest load F=2 N, as demonstrated in Fig. 7a. An extensive investigation of the indent damage evolution revealed five damage modes: inclined cracks, radial cracks, lateral cracks, edge cracks, and shear steps. One of the most significant damage modes was inclined

Fig. 8 SEM micrographs showing Vickers indents of TiN-coated substrates under different loads (di = diameter of Vickers indent and hf = indent depth): **a** F = 2 N, **b** F = 20 N, **c** F = 50 N, and **d** F = 100 N
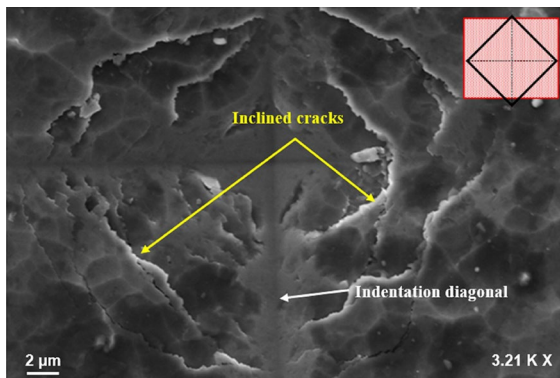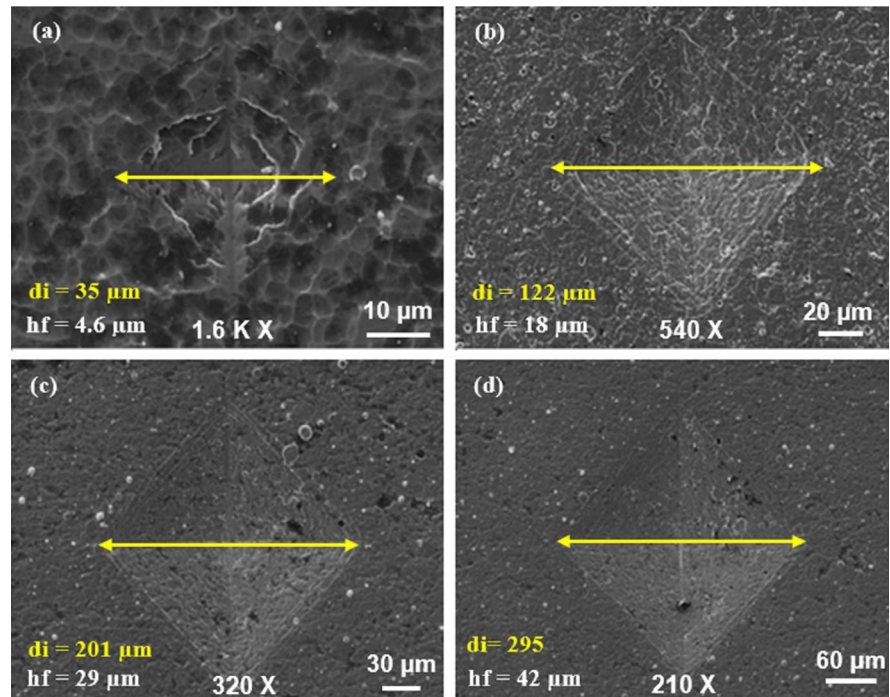

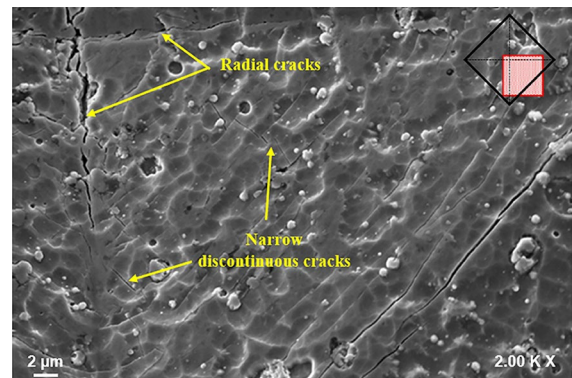**Fig. 9** SEM micrograph: inclined crack damage mode inside Vickers indents at F = 2 N

Fig. 10 SEM micrograph: radial crack and narrow discontinuous crack damage modes inside Vickers indents at F = 20 N

cracking, which was detected at the lowest applied load F = 2 N, as shown in Fig. 9. These cracks were supposed to propagate throughout the thickness to the coating/substrate interface according to the findings reported by Bhowmick (Bhowmick et al. 2003). The inclined cracks propagated with an inclined direction to the normal load direction. Figure 10 illustrates the radial crack mode: cracks propagated diagonally. This type of crack was more pronounced at a higher load: F = 20 N. Narrow discontinuous cracks that

propagated perpendicularly to the indent edges were detected when analyzing the center of the indent, as shown in Fig. 11. These types of cracks were spread over the indentation area and thus connected the edge cracks. The narrow discontinuous cracks presented the lateral damage mode. The fourth principal mode was clearly shown at F = 100 N (Fig. 12), the edge cracks, which propagated parallel and nested to the edges of the indent and to the so-called circumferential cracks, as reported in several studies (Peng et al.
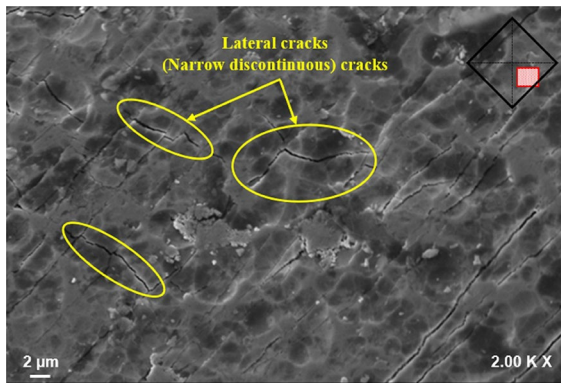
Fig. 11 SEM micrograph: lateral crack damage mode (narrow discontinuous cracks) inside Vickers indents at F = 50 N
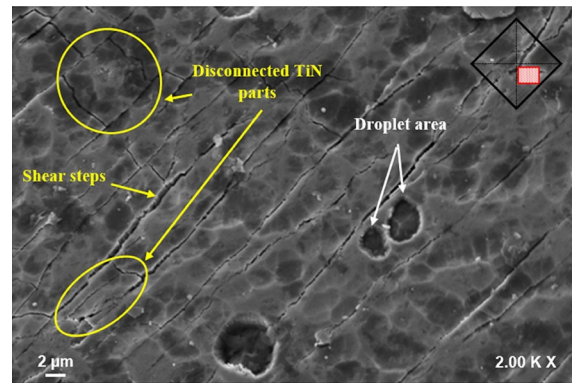

Fig. 13 SEM micrograph: disconnected TiN part and shear step damage modes inside Vickers indents at F = 100 N
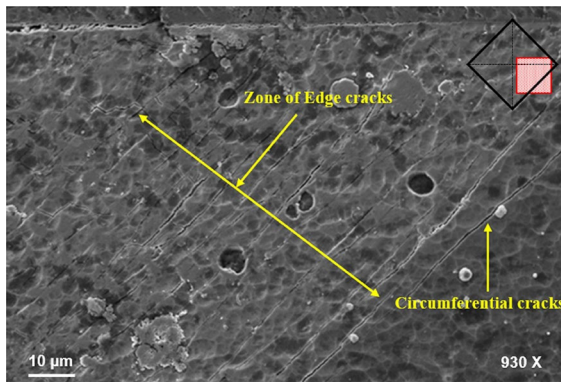

Fig. 12 SEM micrograph: edge crack damage mode inside Vickers indents at F = 100 N

2019). The edge cracks seemed to be equidistant and displayed relatively large spaces between each other. Note that the connection of the lateral cracks with the edge cracks could lead to the partial disconnection of the TiN coating, as presented in Fig. 13. Furthermore, the shear steps in Fig. 13 were the result of the shear stress created under the indenter. These cracks were initiated at the top surface of the coating. The high tensile stress concentration caused by the sharp Vickers indenter could be the principal factor leading to crack initiation at the coating surface. The various applied loads directly affected the development of the different types of damage occurring throughout the TiN coating. Based on the different damage modes discussed previously, we deduced that each applied load led to a specific damage mode or a mixture of two or more modes. The interactions between

two or more damage modes could create additional damage modes, depending on the applied normal load. Moreover, the interaction between the different modes might generate a crack network throughout the coating.

3.1.3 TiN coating under the Brinell indentation test

Brinell indentations at loads between F = 10 N and F = 613 N were investigated in this section. The respective load–unload indentation curves are shown in Fig. 14. The superposition of the different load–unload curves presented good consistency, except for the maximum applied load F = 613 N. This result could have occurred due to the crack network that was spread throughout the coating. The minimum applied load F = 10 N and the maximum applied load F = 613 N resulted in average maximum penetrations of 1.42 μm and 40 μm, respectively.

Figure 15 presents the SEM micrographs of the indentation area. The coating indents showed smooth morphologies. Further SEM investigations confirmed that no cracks were detected at the top surface of the coating until a load of F = 307 N was reached, as illustrated in Fig. 16a. When analyzing Fig. 16b, under a load of F = 613 N, some circular cracks propagated near the center and at the border of the indent. Based on the literature (Bhowmick et al. 2003), performing an indentation using a spherical indenter on a coating deposited on ductile material should result in a compressive stress underneath the indenter and a tensile stress at the indent border throughout the load direction. This phenomenon was proven for thick

Fig. 14 Load–unload
curves of TiN of Brinell
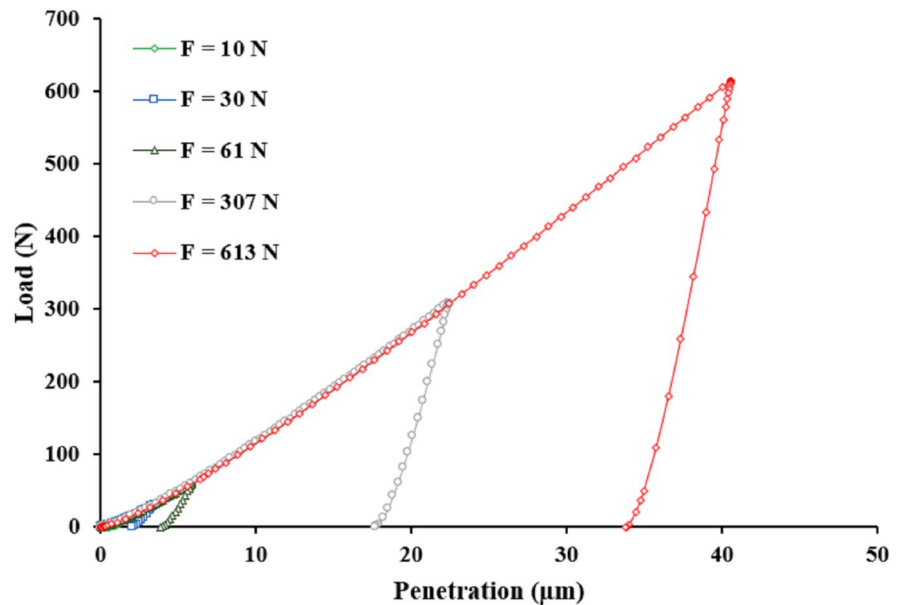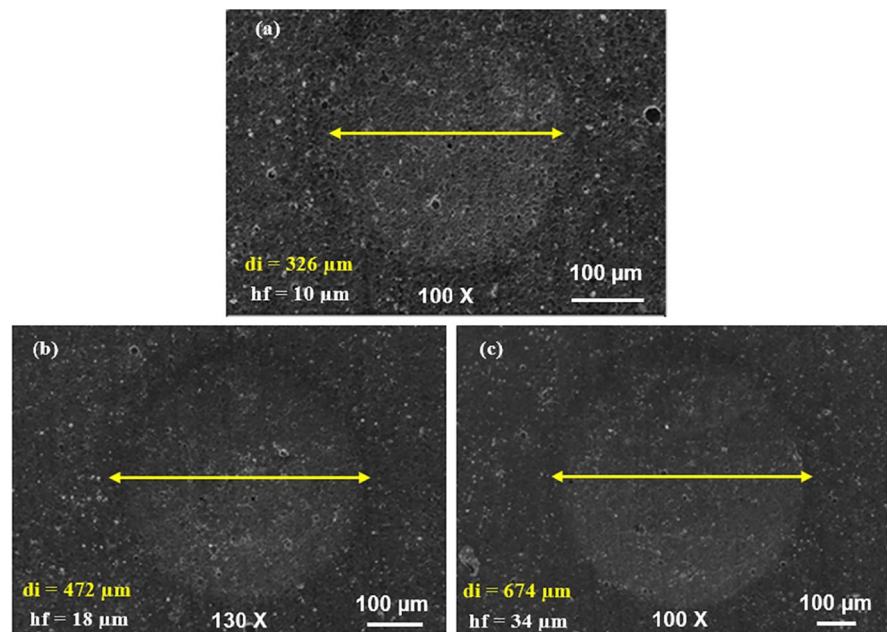indentation tests at loads
varying from F = 10 N to
F = 613 N

Fig. 15 SEM micrographs
showing Brinell indents of
the TiN-coated substrate at
**a** F = 153 N, **b** F = 307 N,
and **c** F = 613 N

(Ma et al. 1995) and thin (Knight et al. 1989) coatings. Furthermore, the damage observed inside the indent was the result of compressive stress (Matthew et al. 1999). As a consequence, cracks were probably initiated at the coating/substrate interface and then propagated in the direction of the top surface of the coating. The intersections of the different cracks consequently generated a remarkable crack network.

Comparable results were found in (Kot et al. 2013; Bhowmick et al. 2003) using a spherical indenter on TiN deposited on stainless steel X2CrNi18-9.

Note that the Brinell tests at a wide range of loads showed different damage modes than the Vickers tests. This phenomenon could have occurred due to the differences in stress concentrations and distributions in the coating/substrate system caused by the

Fig. 16 SEM micrographs showing Brinell indents of TiN-coated substrate at: **a** F = 307 N no cracks and plastic deformation and **b** F = 613 N cracks propagated throughout the coating
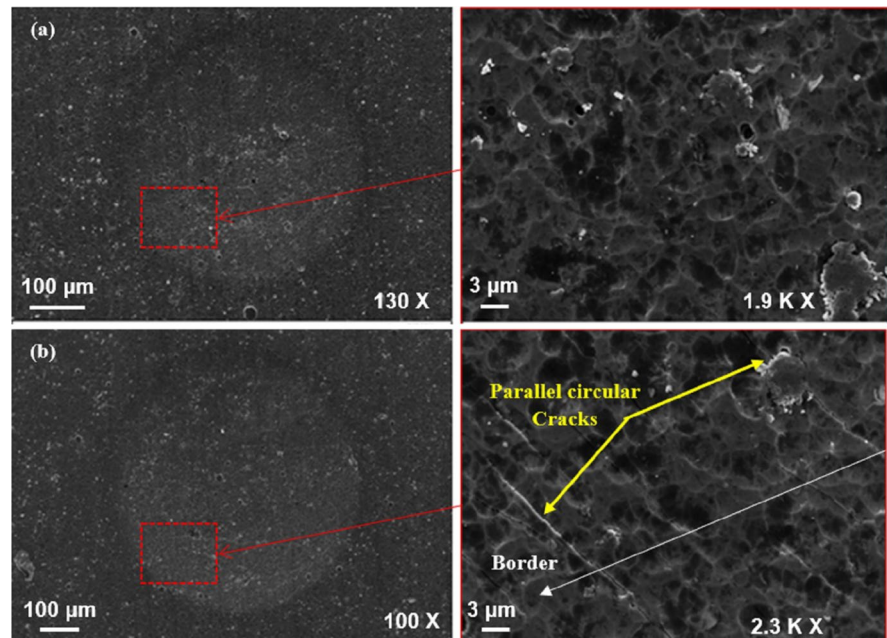
different indenter shapes, as mentioned in a previous study (Bahri et al. 2019).

Few researchers focused on investigating the damage and cracking phenomena throughout the coating surface (Bhowmick et al. 2003; Matthew et al. 1999); the researchers did not consider that the damage of the coating was controlled by single cracks. The investigated damage modes in this study could be considered as a complex interaction of cracks. Based on the obtained results, crack propagation was a three-dimensional network of interacting and intersecting cracks.

To better understand the abovementioned influence of the stress distribution on the crack evolution under Brinell indentation, the results of a finite element analysis were presented in the next section.

3.2 Finite element analysis of Brinell indentation

3.2.1 Model validation

In the first step, the overall performance of the numerical model was verified. The analytical contact pressure was calculated and compared with the numerical contact pressure (Fig. 17a). The TiN thickness considered in this model was set to 4.17 μm based on the experimental data. A relatively good fit between both curves was obtained. In fact, the maximum

contact pressures for the numerical and analytical curves were 594.72 MPa and 563.76 MPa, respectively. The difference could be related to the effect of the indenter geometry since it was defined as a discrete rigid body. The comparison between the analytical and numerical results proved the accuracy of the model. Figure 17b represents the maximum σ_{xx} stress distribution throughout the cross-section of the TiN/X2CrNi18-9 system under Brinell indentation tests at a load of F = 0.05 N. The maximum penetration for the aforementioned load was 0.04 μm, corresponding to the Hertz conditions. A stress concentration within the coating was seen where the maximum stress reached σ_{xx} = 49 MPa. The maximum stress recorded for the substrate was σ_{yy} = 0.02 MPa; considering the stress–strain curve, this phenomenon showed that the substrate was still under purely elastic deformation, which was determined by the experimental tensile test.

3.2.2 Correlation between the experimental and numerical Brinell indentation results

Figure 18 shows a comparison of the load–unload curve based on the indentation test and on the finite element analysis at a load of F = 10 N. A relatively good agreement was observed between both curves. The small discrepancy was explained by the

Fig. 17 Numerical model validation under Brinell indentation under a normal load of F = 0.05 N: **a** contact pressure profile and **b** σ_{xx} stress distribution
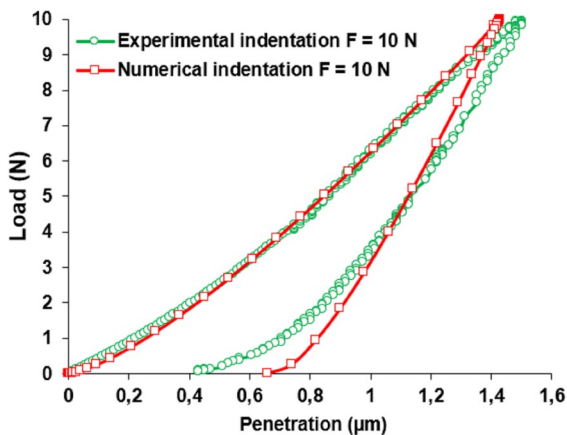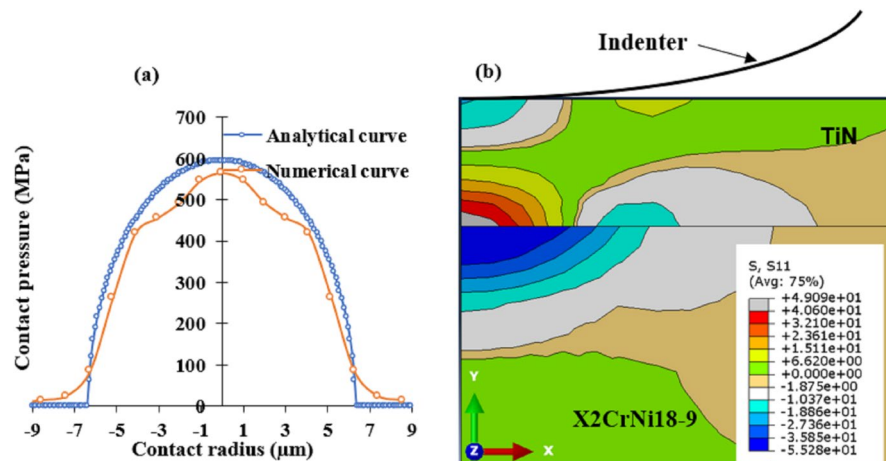

Fig. 18 Comparison between the experimental and numerical load–unload curves of the Brinell indentation test at F = 10 N

roughness of the TiN surface, which was considered in the numerical simulation to be perfectly smooth. Note that during the simulation, the contact between the indenter and the coating surface was considered frictionless. Based on former studies, the friction coefficient affected the load–unload curve during indentation tests (Baoxing et al. 2010; Cao et al. 2007). The friction coefficient may play a role when the penetration of the indenter into the materials is deep to some extent (Tirupataiah et al. 1991; Taljat et al. 2004; Baoxing et al. 2010; Lee et al. 2010). In the present study, the friction coefficient effect was not considered; it will be considered in future work.

In the present section, the results after the load–unload indentation test are presented to understand the residual stress distribution throughout the coating and the substrate. The residual stress recorded after loading was compared to the SEM images and thus led to the first indication of the minimum stress level for crack initiation throughout the coating. As mentioned in the introduction, we assumed that crack initiation occurred during the loading phase at high stress levels. Nevertheless, the first correlation was performed based on the residual stress distribution at the top surfaces of the indents, and crack initiation was seen at the experimental Brinell indents. In addition, the deduced numerical results after loading were then compared with the numerical stress distribution obtained under loading. Figs. 19 and 20 present the numerical stress distribution at the top surface of the coating after indentation at loads of F = 307 N and F = 613 N, respectively. Figure 19a reveals that high residual stresses were at the border and center of the indent. At a load of F = 307 N, the stress at the border was 5735 MPa, and that at the center was 4648 MPa. At this load level, no cracks were detected at the top surface of the TiN coating after indentation. In Fig. 19a, the radius r = 226 μm corresponds to the plastic track where the maximum stress σ_{xx} = 5735 MPa was recorded at the top surface. In Fig. 19b and for the same position r = 226 μm no crack was detected. When analyzing the stress distribution after indentation at the load F = 613 N (Fig. 20a), a residual stress of 8598 MPa was recorded at the center and the border of the indent. Note that at F = 613 N, cracks were detected
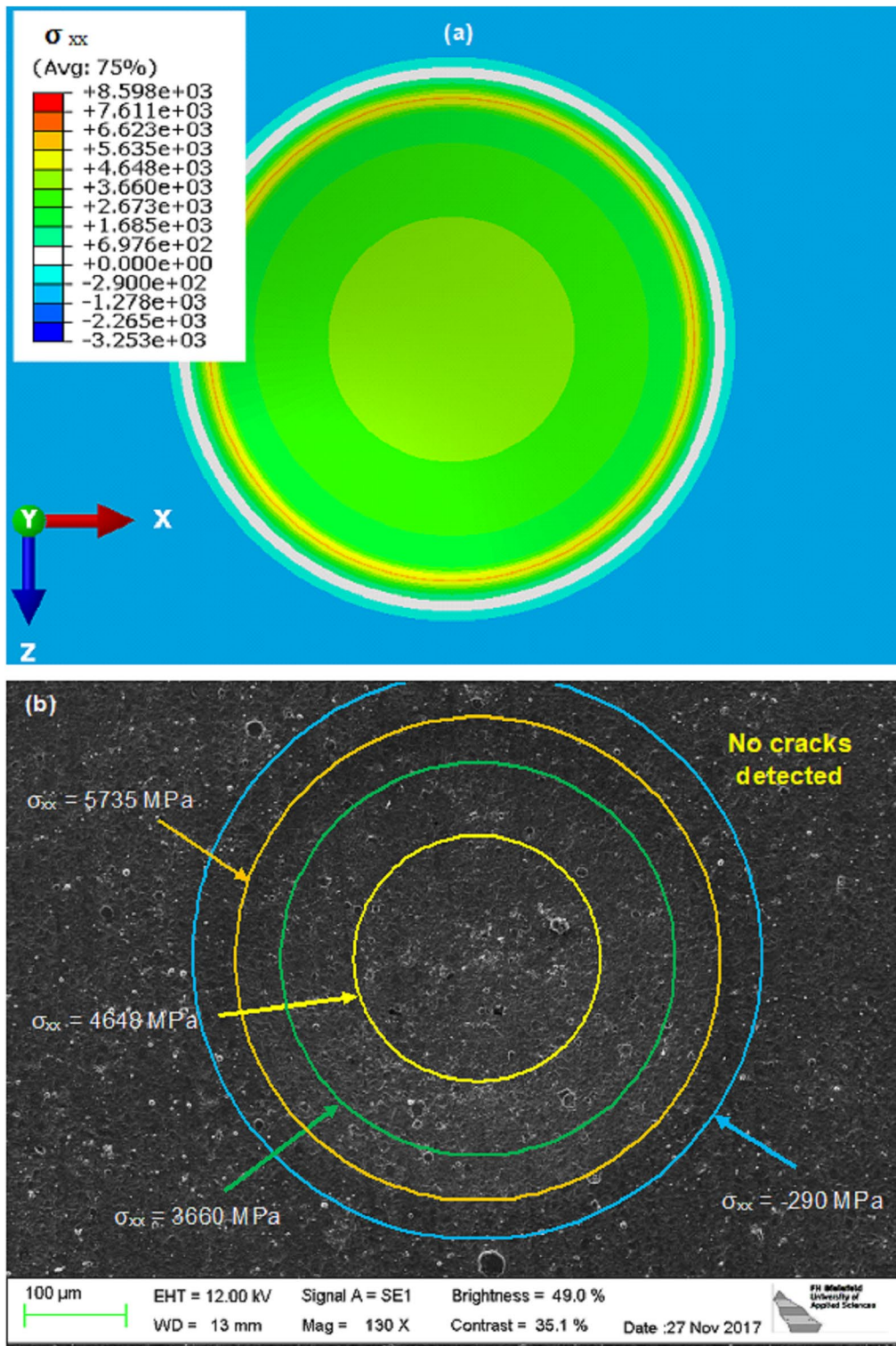
Fig. 19 Brinell indentation test at F=307 N: **a** residual stress distribution (σ_{xx}) at the top surface of the coating based on FEM analysis and **b** SEM micrograph
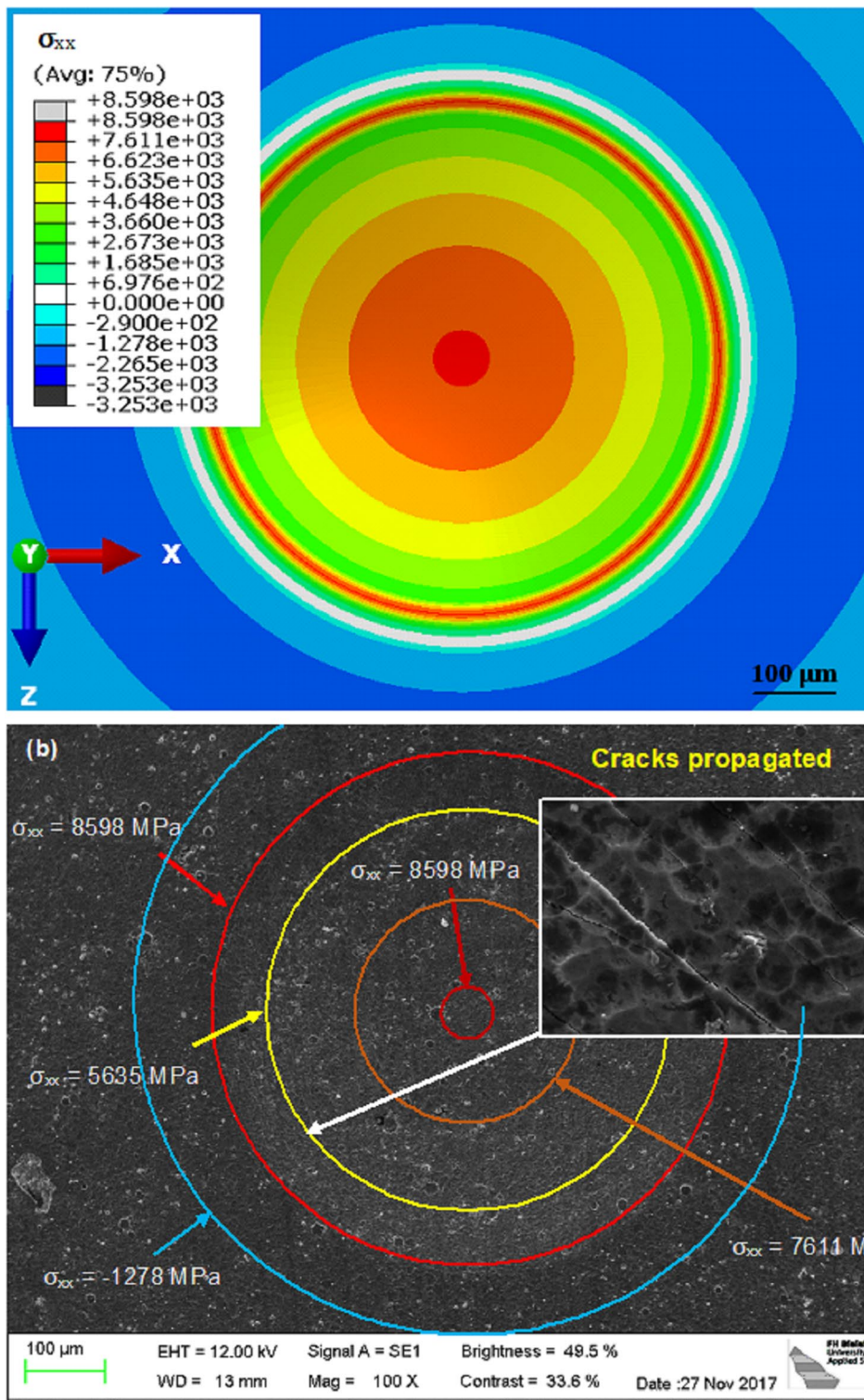
Fig. 20 Brinell indentation test at F=613 N: **a** maximum σ_{xx} stress distribution (σ_{xx}) at the top surface of the coating based on FEM analysis and **b** SEM micrograph
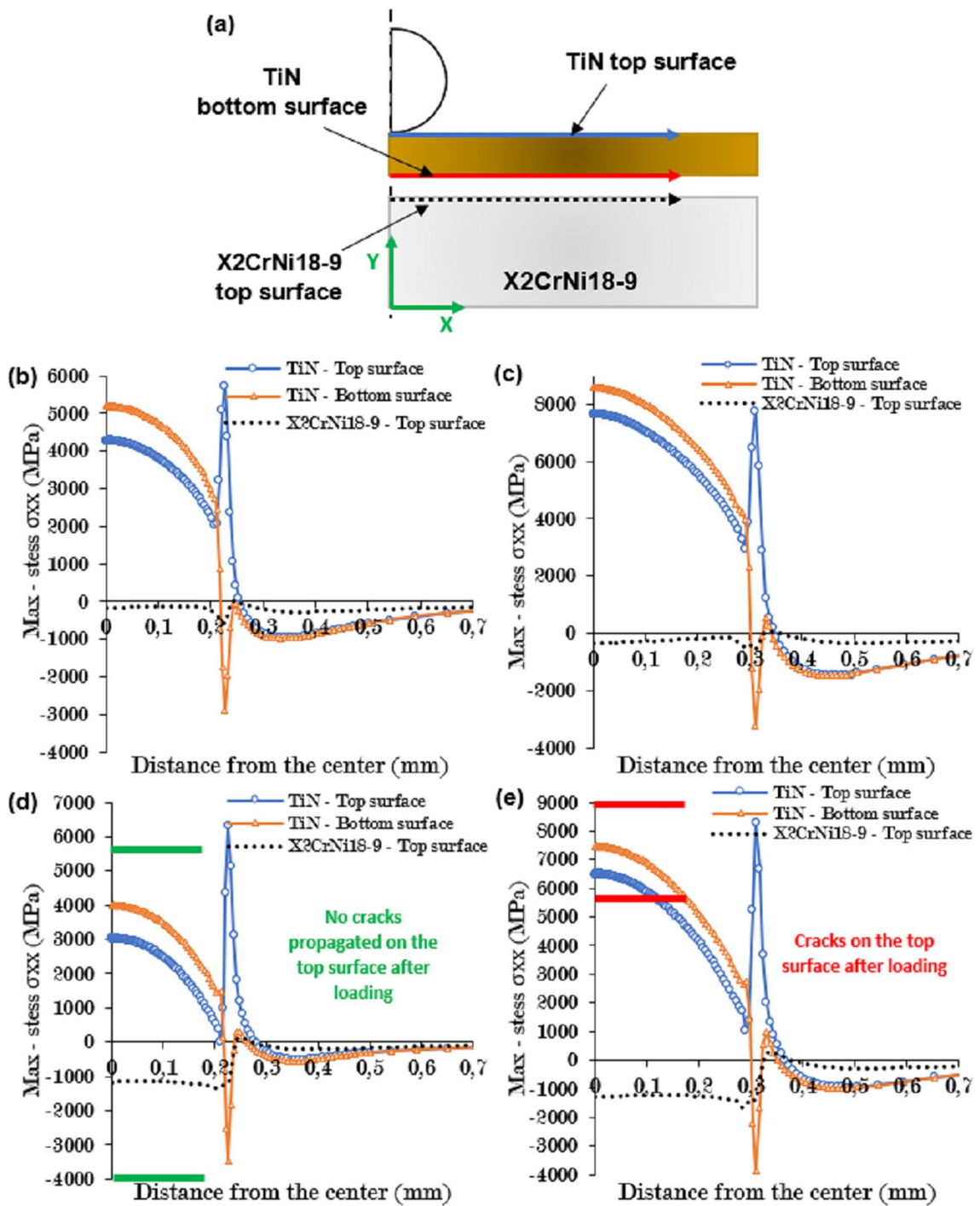
Fig. 21 Stress throughout the x-axis (σ_{xx}): **a** Illustration of the extracted profiles, **b** stress curve after loading: F = 307 N, **c** stress curve after loading: F = 613 N, **d** stress curve under loading: F = 307 N, **e** stress curves under loading: F = 613 N

after loading by SEM at the border and near the middle of the indent, which was in good agreement with

the determined high numerical stresses in these areas. Based on the obtained results, it was assumed that the

Fig. 22 Stress curves along the x-axis (σ_{yy}) at a load of F = 307 N: **a** after loading and **b** under loading
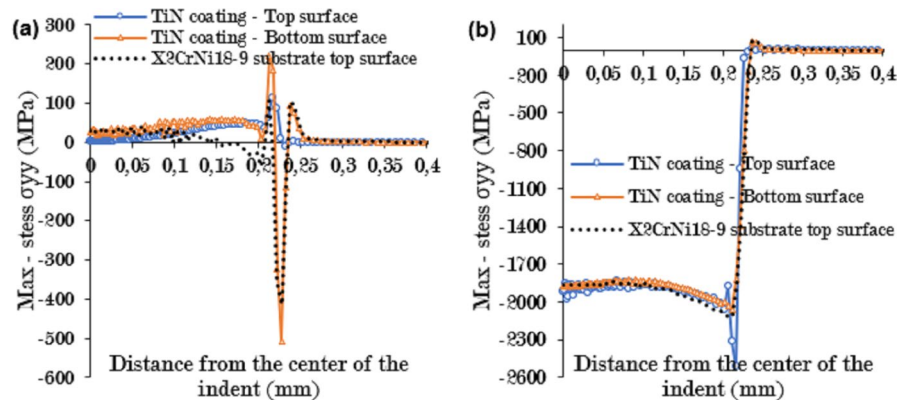
critical stress σ_{xx} should exceed 5735 MPa to initiate damage (Kopernik et al. 2011; Kopernik et al. 2014).

To understand that the damage occurred throughout the TiN coating and to localize the stress concentration areas, the residual stress distribution after loading and the stress distribution under loading were extracted from the numerical simulations (Fig. 21). Figure 21a presents three extracted curves, namely, the curve at the top surface of the coating, at the bottom surface of the coating, and at the top surface of the substrate. Figure 21b and Fig. 21c show the residual stress evolution σ_{xx} through the x-axis after a normal load of F = 307 N and F = 613 N. A high tensile stress level was recorded at the top surface of the coating, in the center of indent and at the border with the highest values. Outside the indent, a compressive residual stress was seen. Moreover, the curve of the bottom surface revealed a tensile stress at the center of the indent and a compressive stress at the border. The highest stress at the bottom surface was recorded in the center of the indent, which was even higher than the stress at the top surface. This phenomenon could cause crack initiation at the interface between the coating and the substrate. At the border of the indent, the maximum stress was recorded at the top surface of the coating, which could have led to crack initiation at the top surface.

Assuming that the first crack initiation occurred during loading, the maximum stress σ_{xx} under load presented in Fig. 21d and e showed the stress concentrations in both coating and substrate. Figure 21d shows that at a load of F = 307 N, the tensile stresses in the center of the indent at the top and bottom surfaces of the coating reached $\sigma_{xx} = 3000$ MPa and $\sigma_{xx} = 4000$ MPa, respectively. Moreover, the stress

evolution throughout the substrate showed a compressive stress $\sigma_{xx} = -1162$ MPa. The highest stress was recorded at the border of the indent at the top surface of the coating with a tensile stress level of $\sigma_{xx} = 6317$ MPa. However, at the bottom surface of the coating, the stress was determined to be a compressive stress of $\sigma_{xx} = -3457$ MPa. According to the SEM investigations presented in Fig. 16a, no cracks were detected at the top surface of the coating. When analyzing the three σ_{xx} stress curves presented in Fig. 21e under a normal load F = 613 N, the same trend was observed. The stresses at the center of the indent reached $\sigma_{xx} = 6490$ MPa and $\sigma_{xx} = 7474$ MPa on the bottom and top surfaces, respectively. Under this load based on the SEM investigations provided in Fig. 16b, cracks could be detected at the top surface of the coating, creating a crack network. When comparing the stress levels after loading and under loading at loads of F = 307 N and F = 613, we noted that the stress level after unloading at the center of the indent was higher than that under loading in both cases. Moreover, the stress level at the border of the indent presented higher values under loading than after loading. The presented phenomena could be explained by the fact that the pure elastic behavior of the coating was influenced by the elastic−plastic deformation of the substrate.

Figure 22 shows the stress evolution σ_{yy} throughout the x-axis after loading and under loading. At loads of F = 307 N and F = 613 N (Fig. 22a), the maximum residual stress recorded was $\sigma_{yy} = -506$ MPa at the border of the indents. The changes in the residual stress from tensile to compressive at the border could be related to the pile-up phenomena mentioned in a previous study (Bahri et al. 2019) and are

generated due to the large Young's modulus/yield stress ratio of the substrate. The stress σ_{yy} under loading is presented in Fig. 22b. The stress evolution σ_{yy} revealed that the coating was exposed to compressive loads. The absolute stress level in the y direction (σ_{yy}) was lower than that in the xx direction (σ_{xx}), showing the importance of the σ_{xx} stress distribution for crack initiation.

4 Conclusions

In the present study, a TiN coating was deposited on stainless steel X2CrNi18-9 using cathodic arc physical vapor deposition (CAPVD). Vickers and Brinell indentation tests with load ranges from F = 2 N to F = 200 N and F = 10 N to F = 613 N, respectively, were carried out; the indents were subsequently investigated by SEM to determine the damage modes occurring throughout the coating. The main results were as follows:

The indentations performed by Vickers tests revealed five damage modes: lateral cracks, radial cracks, edge cracks, inclined cracks, and shear steps. Furthermore, based on the obtained results, the cracks could be initiated at the coating/substrate interface as a result of tensile stresses and then propagated in the direction of the top surface of the coating.

As a result of the Brinell indentation tests, the damage mode in form of circular cracks caused by tensile stresses occurred at the border and the center of the indent. At the center, cracks could initiate at the interface coating/substrate; at the border, cracks could start from the top surface of the substrate to the coating/substrate interface. This damage was detected at a load exceeding F = 307 N.

The increase in the applied loads by using Vickers and Brinell indentation testing influenced the damage modes of the coating. Especially under Vickers indents, all applied loads generated one or more crack modes, which could then interact to create further damage modes when increasing the normal load.

Comparing the Vickers and Brinell indentations regarding damage propagation under high loads, it was concluded that Brinell indentation tests were seemingly more appropriate for characterizing the damage modes since Vickers indentation

tests resulted in damage within the whole load range applied in the actual study.

The correlation between the numerical and experimental Brinell indentation results revealed that the TiN coating started to fail at a maximum residual σ_{xx} stress higher than 5735 MPa, as determined after loading. Furthermore, the numerical results showed that cracks were initiated at the border of the indent at the top surface of the coating and in the center of the indent at the bottom surface of the coating. Furthermore, the numerical simulation showed that the cracks that occurred during the Brinell indentation test were mainly caused by tensile stresses in the x-direction.

In further finite element investigations, the main objectives would be to introduce a damage model to the TiN coating and to analyze the friction coefficient and the thickness effects on the damage behavior of the coating.

Data availability statements The data that support the findings of this study are available from the corresponding author upon reasonable request.

Declarations

Conflict of interest The authors declare that they have no conflicts of interest.

References

Arulkirubakaran, D., Senthil Kumar, V.: Performance of TiN and TiAlN coated micro-grooved tools during machining of Ti–6Al–4V alloy. Int. J. Refract. Metals Hard Mater. **62**, 47–57 (2017)

Bahri, A., Guermazi, N., Elleuch, K., Ürgen, M.: Tribological performance of TiN coatings deposited on 304 L stainless steel used for Olive-oil extraction. Wear **342–343**, 77–84 (2015)

Bahri, A., Kaçar, E., Akkaya, S.S., Elleuch, K., Ürgen, M.: Wear protection potential of TiN coatings for 304 stainless steels used in rotating parts during olive oil extraction. Surf. Coat. Technol. **304**, 560–566 (2016a)

Bahri, A., Guermazi, N., Elleuch, K., Ürgen, M.: On the erosive wear of 304 L stainless steel caused by olive seed particles impact: modeling and experiments. Tribol. Int. **102**, 608–619 (2016b)

Bahri, A., Ellouz, M., Klöker, M., Kordisch, T.: Indentation behavior of stainless steel 304 L coated with TiN and TiAlN. In: MSE conference (2018)—Material science and Engineering Darmstadt Germany (2018). https://doi.org/10.13140/RG.2.2.22068.07047

Bahri, A., Ellouz, M., Klöcker, M., Kordisch, T., Elleuch, K.: Brinell indentation behavior of the stainless steel X2CrNi18-9: Modeling and experiments. Int. J. Mech. Sci. **163**, 105142 (2019)

Baoxing, X.: Determining engineering stress-strain curve directly from the load-depth curve of spherical indentation test. J. Mater. Res. **25**, 2297–2307 (2010)

Begley, M.R., Evans, A.G., John, W.: Hutchinson, Spherical impression of thin elastic films on elastic-plastic substrates. Int. J. Solids Struct. **25**, 1662–1677 (1999)

Bell, T., Mao, K., Sun, Y.: Surface engineering design: modelling surface engineering systems for improved tribological performance. Surf. Coat. Technol. **108–109**, 360–368 (1998)

Bhowmick, S., Kale, A.N., Jayaram, V., Biswas, S.K.: Contact damage in TiN coatings on steel. Thin Solid Films **436**, 250–258 (2003)

Bobzin, K.: High-performance coatings for cutting tools. CIRP J. Manuf. Sci. Technol. **18**, 1–9 (2017)

Cao, Y., Qian, X., Huber, N.: Spherical indentation into elastoplastic materials: indentation-response based definitions of the representative strain. Mater. Sci. Eng. A **454–455**, 1–13 (2007)

Dejun, K., Guizhong, F.: Nanoindentation analysis if TiN, TiAlN and TiAlSiN coatings prepared by cathode Ion plating. Technol. Sci. **58**, 1360–1368 (2015)

Ducobu, F., Rivière-Lorphèvre, E., Filippi, E.: Finite element modelling of 3D orthogonal cutting experimental tests with the coupled Eulerian-Lagrangian (CEL) formulation. Finite Elem. Anal. Des. **134**, 27–40 (2017)

Faisal, N.H., Prathuru, A.K., Goel, S., Ahmed, R., Droubi, M.G., Beake, D.B., Fu, Y.Q.: Cyclic nanoindentation and nano-impact fatigue mechanisms of functionally graded TiN/TiNi film. Shape Mem. Super Elast. **3**, 149–167 (2017)

Harris, S.G., Doyle, E.D., Wong, Y.C., Munroe, P.R., Cairney, J.M., Long, J.M.: Reducing the macroparticle content of cathodic arc evaporation TiN coatings. Surf. Coat. Technol. **183**, 283–294 (2004)

Johnson, K.L.: Contact mechanics. Cambridge University Press (1987)

Jianxin, D., Fengfang, W., Yunsong, L., Youqiang, X., Shipeng, L.: Erosion wear of CrN, TiN, CrAlN, and TiAlN PVD nitride coatings. Int. J. Refract. Met. Hard Mater. **35**, 10–16 (2012)

Knight, J.C., Page, T.F., Hutchings, I.M.: Surface deformation behaviour of tic and tin coated steels: 1 indentation response. Surf. Eng. **5**(3), 213–225 (1989)

Kim, J.-H., Paulino, G.H.: Simulation of crack propagation in functionally graded materials under mixed-mode and nonproportional loading. Int. J. Mech. Mater. Des. **1**, 63–94 (2004)

Koike, A., Akiba, S., Sakagami, T., Hayashi, K., Ito, S.: Difference of cracking behavior due to Vickers indentation between physically and chemically tempered glasses. J. Non-Cryst. Solids **358**(24), 3438–3444 (2012)

Kopernik, M., Milenin, A., Major, R., Lackner, J.M.: Identification of material model of TiN using numerical simulation of nano-indentation test. Mater. Sci. Technol. **27**(3), 604–616 (2011)

Kopernik, M., Milenin, A.: Numerical modeling of substrate effect on determination of elastic and plastic properties of TiN nanocoating in nanoindentation test. Arch. Civ. Mech. Eng. **I**(4), 269–277 (2014)

Kot, M., Rakowski, W., Lackner, J.M., Major, Ł: Analysis of spherical indentations of coating-substrate systems: experiments and finite element modeling. Mater. Des. **43**, 99–111 (2013)

Lee, K.S., Wuttiphan, S., Hu, X.Z., Lee, S.K., Lawn, B.R.: Contact-induced transverse fractures in brittle layers on soft substrates: a study on silicon nitride bilayers. J. Am. Ceram. Soc. **81**(3), 571–580 (1998)

Lee, J.H., Kim, T., Lee, H.: A study on robust indentation techniques to evaluate elastic–plastic properties of metals. Int. J. Solids Struct. **47**, 647 (2010)

Liu, A., Deng, J., Cui, H., Chen, Y., Zhao, J.: Friction and wear properties of TiN, TiAlN, AlTiN and CrAlN PVD nitride coatings. Int. J. Refract. Metals Hard Mater. **31**, 82–88 (2012)

Ma, K.J., Bloyce, A., Bell, T.: Examination of mechanical properties and failure mechanisms of TiN and Ti–TiN multilayer coatings. Surf. Coat. Technol. **76–77**, 297 (1995)

Martinez-Paneda, E., Gallego, R.: Numerical analysis of quasi-static fracture in functionally graded materials. Int. J. Mech. Mater. Des. **11**, 405–424 (2015)

Pantel, A.M., Fontaine, M., Thibaud, S., Gelin, J.C.: 3D FEM of shoulder milling operation on a 304 L stainless steel. Simul. Model Pract. Theory **22**, 13–27 (2012)

Perzynski, K., Majed, L.: Numerical modeling of fracture during nano indentation of TiN coating obtained with the PLD process. Tech. Sci. **61**, 973–978 (2013)

Peng, S., Xu, J., Munroe, P., Xie, Z.: Sandwich-structured, damage-resistant TiN/graded TiSiN/TiSiN film. Results Phys. **12**, 543–554 (2019)

Rabe, R., Breguet, J.M., Schwaller, P., Stauss, S., Haug, F.J., Patscheider, J., et al.: Observation of fracture and plastic deformation during indentation and scratching inside the scanning electron microscope. Thin Solid Films **469–470**, 206–213 (2004)

Ren, H.L., Zhuang, X.Y., Anitescu, C., Rabczuk, T.: An explicit phase field method for brittle dynamic fracture. Comput. Struct. **217**, 45–56 (2019)

Singh, I.V., Mishra, B.K., Bhattacharya, S.: XFEM simulation of cracks, holes and inclusions in functionally graded materials. Int. J. Mech. Mater. Des. **7**, 199–218 (2011)

Ren, H., Zhuang, X., Rabczuk, T.: A higher order nonlocal operator method for solving partial differential equations. Comput. Methods Appl. Mech. Eng. **367**, 113132 (2020)

Richter, J.: Application of Vickers indentation for assessment of PVD TiN coated new nonledeburitic high-speed steels. Surf Coat Technol **162**, 119–130 (2003)

Taljat, B., Pharr, G.M.: Development of pile-up during spherical indentation of elastic–plastic solids. Int. J. Solids Struct. **41**, 3891 (2004)

Tasdemirci, A., Sahin, S., Kara, A., Turan, K.: Crushing and energy absorption characteristics of combined geometry shells at quasi-static and dynamic strain rates: experimental and numerical study. Thin-Walled Struct. **86**, 83–93 (2015)

Tirupataiah, Y.: On the constraint factor associated with the indentation of work-hardening materials with a spherical ball. Metall. Trans. A **22**, 2375 (1991)

Vadiraj, A., Kamaraj, M.: Characterization of fretting fatigue damage of PVD TiN coated biomedical titanium alloys. Surf. Coat. Technol. **200**, 4538–4542 (2006)

Vereschaka, A.A., Grigoriev, S.N., Sitnikov, N.N., Oganyan, G.V., Batako, A.: Working efficiency of cutting tools with multilayer nano-structured Ti-TiCN (Ti, Al) CN and Ti-TiCN-(Ti, Al, Cr)CN coatings: analysis of cutting properties, wear mechanism and diffusion processes. Surf. Coat. Technol. **332**, 198–213 (2017)

Weppelmann, E.R., Hu, X.Z., Swain, M.: Observation and simple fracture mechanics analysis of indentation fracture delamination of TiN films on silicon. J Adhes Sci Technol **8**(6), 611–624 (1994)

Wo, P.C., Munroe, P.R., Zhou, Z.F., Li, K.Y., Xie, Z.H.: Effects of TiN sublayers on the response of TiSiN nanocomposite coatings to nanoidentation and scratching contacts. Mater. Sci. Eng. A **527**, 4447–4457 (2010)

Yongqiang, W., Xiaoya, Z., Zhiqiang, J., Xiubo, T.: Characterization and mechanical properties of TiN/TiAlN multilayer coatings with different modulation periods, Int. J. Adv. Manuf. Technol. 1–7 (2017).

Zhang, Y., Zhuang, X.: Cracking elements method for dynamic brittle fracture. Theor. Appl. Fract. Mech. **102**, 1–9 (2019)

Zhang, Y., Huang, J., Yuan, Y., Mang, H.: A, Cracking elements method with a dissipation-based arc-length approach. Finite Elem. Anal. Des. **195**, 103573 (2021)